

Noninvasive assessment of intracranial pressure in dogs by use of biomechanical response behavior, diagnostic imaging, and finite element analysis

Adrienne M. Madison PhD

Ajay Sharma DVM

Mark A. Haidekker PhD

Received February 28, 2014.

Accepted December 22, 2014.

From the College of Engineering (Madison, Haidekker) and Department of Veterinary Bioscience and Diagnostic Imaging, College of Veterinary Medicine (Sharma), University of Georgia, Athens, GA 30602. Dr. Madison's present address is 862 Park Ave, Fairfield, AL 35064.

Address correspondence to Dr. Sharma (as7930@uga.edu).

OBJECTIVE

To develop a novel method for use of diagnostic imaging, finite element analysis (FEA), and simulated biomechanical response behavior of brain tissue in noninvasive assessment and estimation of intracranial pressure (ICP) of dogs.

SAMPLE

MRI data for 5 dogs.

PROCEDURES

MRI data for 5 dogs (1 with a geometrically normal brain that had no detectable signs of injury or disease and 4 with various degrees of geometric abnormalities) were obtained from a digital imaging archiving and communication system database. Patient-specific 3-D models composed of exact brain geometries were constructed from MRI images. Finite element analysis was used to simulate and observe patterns of nonlinear biphasic biomechanical response behavior of geometrically normal and abnormal canine brains at various levels of decreasing cerebral perfusion pressure and increasing ICP.

RESULTS

Changes in biomechanical response behavior were detected with FEA for decreasing cerebral perfusion pressure and increasing ICP. Abnormalities in brain geometry led to observable changes in deformation and biomechanical response behavior for increased ICP, compared with results for geometrically normal brains.

CONCLUSIONS AND CLINICAL RELEVANCE

In this study, patient-specific critical ICP was identified, which could be useful as a method to predict the onset of brain herniation. Results indicated that it was feasible to apply FEA to brain geometry obtained from MRI data of clinical patients and to use biomechanical response behavior resulting from increased ICP as a diagnostic and prognostic method to noninvasively assess or classify levels of brain injury in clinical veterinary settings. (*Am J Vet Res* 2015;76:667–678)

Intracranial pressure is a balance between volumes of the brain parenchyma, blood, and CSF in the cranial cavity. Uncompensated increases in the volume of any of these components will cause increases in ICP. Maintenance of brain function is dependent on blood flow to the brain and is affected regardless of whether the increase in ICP is a result of an increase in the volume of brain tissue, blood, or CSF. The relationship between brain function, blood flow, and ICP is attributed to alterations in the CPP, which is a conceptual pressure balance between systemic MAP and ICP. The CPP is calculated as $CPP = MAP - ICP$. The MAP is calculated as $MAP = ([2 \times DAP] + SAP)/3$, where DAP is diastolic arterial blood pressure and SAP is systolic arterial blood pressure.

ABBREVIATIONS

CCBD	Cranial cavity boundary interface
CPP	Cerebral perfusion pressure
FEA	Finite element analysis
ICP	Intracranial pressure
MAP	Mean arterial blood pressure

Intracranial pressure in humans can be classified as normal (5 to 15 mm Hg), increased (20 to 30 mm Hg), sustained (> 20 mm Hg for > 5 minutes), or severe (> 40 mm Hg).^{1,2} The reference range for ICP in clinically normal dogs ranges from 0.67 to 1.60 kPa (5 to 12 mm Hg).³ Increased ICP, especially sustained and severe states, is a serious medical problem that can lead to brain and spinal cord damage as a result of pressure on brain structures and restriction of blood flow to the brain. Severe or sustained increases in ICP can lead to permanent neurologic problems such as seizure or stroke and, in extreme cases, can cause death. Causes of increases in ICP attributable to illnesses, disorders, and impact injuries can be classified within 2 general categories.⁴ Brain hemorrhage, a vascular cause of increased ICP, is classified as active in the presence of arterial distention or dilation and passive in the presence of venous obstruction. Nonvascular causes of increased ICP can be attributed to increases in brain

bulk (edema); mass effects such as a tumor, abscess, or hematoma; and accumulations of CSF as a result of flow obstructions or absorption impediments.

The brain responds physiologically to increases in ICP. This response is classified as levels I to IV (**Appendix I**). In levels I and II, the brain's autoregulatory mechanism compensates for mild or transient increases in ICP and maintains the CPP in homeostasis. In levels III and IV, prolonged or rapid increases in ICP overwhelm the compensatory responses and lead to severe decompensation and failure to maintain adequate CPP. Permanent brain injury and death are almost always inevitable with increased ICP at level IV. Early, accurate, and noninvasive assessment and monitoring of increased ICP at levels I and II are essential for effective treatment and prevention of irreversible brain injury.

The general nonlinear pressure-volume relationship of all components of the cranial cavity allows determination of the compliance, a measure of volume distensibility.^{5,a} The compliance coefficient is calculated as $\phi = \Delta V / \Delta P$, where ΔV is change in volume and ΔP is change in pressure. The compliance coefficient is the reciprocal slope of the curve and is dependent on the component of the cranial cavity for which the volume is increasing (**Figure 1**). In addition, onset of nonlinearity of the curve corresponds to the decompensation levels (levels III and IV) at which ICP is high and the brain's autoregulation mechanisms cease to be effective.

Intracranial pressure monitoring can be performed by invasive or noninvasive methods. Invasive methods are more accurate, but they require surgical insertion of pressure sensors by trained specialists and are associated with risks of infection, hemorrhage, and iatrogenic brain and spinal cord damage.⁶⁻¹⁰ Diagnostic imaging modalities are valuable assets that allow visual qualitative identification and assessment of phenomena known to contribute to increases in ICP. To our knowledge, no noninvasive method has been successfully integrated into ICP monitoring in clinical practice. This can be attributed to uncertainties related to the accuracy and validity of the measurements obtained. Biomechanical models can assist in the noninvasive estimation of ICP. The earliest simulations of the cranial cavities used simplified mathematical models to derive solutions that expressed the nonlinear relationships between pressure, volume, volume-pressure responses, and compliance.¹¹⁻¹⁵

Finite element modeling is rapidly gaining popularity for use in the evaluation of the biomechanical response behavior of biological tissues. For noninvasive studies, diagnostic imaging methods, such as CT or MRI, are used to ascertain the anatomic geometry. Nonlinear biphasic 3-D finite element models that incorporate brain parenchyma and ventricular geometry obtained from diagnostic images of human and various animal species have been used to analyze the deformation and constitutive behavior of brain tissue in response to ICP.¹⁶⁻²¹ However, none of the methods

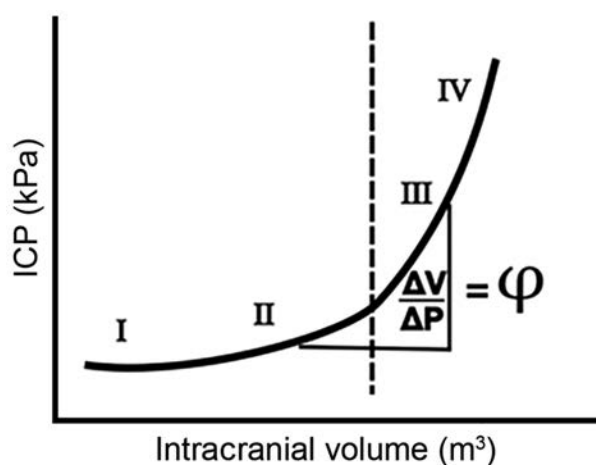


Figure 1—Graph of the curve for changes in intracranial volume versus ICP. The volume-pressure relationship is linear in levels I and II because of the brain's autoregulation compensation mechanisms that maintain equilibrium. These mechanisms become overwhelmed at the critical volume (vertical dashed line), which subsequently results in a nonlinear relationship. Decompensation responses for levels III and IV are the result of substantial increases of ICP. The compliance coefficient ($\phi = \Delta V / \Delta P$, where ΔV is change in volume and ΔP is change in pressure) is the reciprocal slope of the pressure-volume curve and measures volume distensibility for all components contained in the cranial cavity.

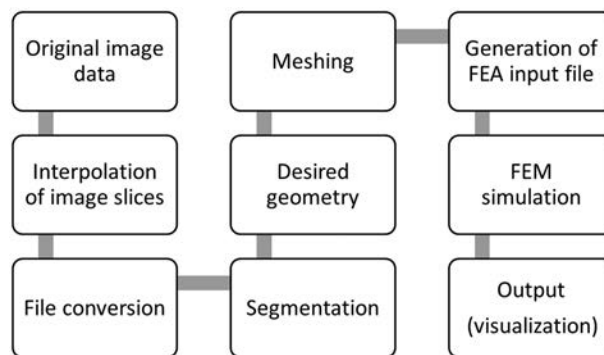


Figure 2—Schematic representation of the experimental process for FEA analysis of diagnostic imaging data for estimation of ICP. FEM = Finite element model.

use biomechanical response behavior to assess, derive, or estimate ICP from clinically available diagnostic imaging data obtained for canine patients with assorted types and severity of brain injuries.

The purpose of the study reported here was to describe a noninvasive method to estimate ICP and other critical values by use of FEA; mathematical relationships between pressure, volume, stress, and strain; and 3-D brain models obtained from diagnostic imaging data. On the basis of the relationships between the CPP and ICP, patterns of nonlinear biomechanical response behavior were determined by use of biphasic analysis of geometrically normal (no signs of injury or disease detectable on imaging data) and abnormal canine brains. The method relied on the material re-

sponse behavior by the brain parenchyma as a result of increased ICP. The goal was to establish a proof-of-principle framework that could eventually be used in clinical settings for noninvasive patient-specific assessment of ICP by use of changes in biomechanical property values obtained from diagnostic medical imaging data and FEA.

Materials and Methods

Sample

Sets of MRI data for 5 dogs were used for the study. One of the dogs was clinically normal (dog 1; image dimensions, 512 X 512 X 23 voxels), and the other 4 dogs had abnormalities, which included congenital occipital malformation with hydrocephalus and syringohydromyelia (dog 2; image dimensions, 512 X 512 X 9 voxels), cystic meningioma in the ventral aspect of the cranial cavity (dog 3; image dimensions, 512 X 512 X 23 voxels), cerebellar mass with cerebellar herniation (dog 4; image dimensions, 512 X 512 X 23 voxels), and meningioma in the rostral aspect of the cranial cavity (dog 5; image dimensions, 512 X 512 X 25 voxels). Imaging data were obtained from a digital imaging archiving and communication system database. The final diagnostic imaging report, medical record, or necropsy results were used to confirm the medical conditions reported.

Image acquisition

On the basis of MRI data, a volumetric image composed of cross-sectional slices was used to define the geometry of the skull, brain, and CSF spaces for FEA (**Figure 2**). Data for 2-D sagittal T2 spin-echo sequence MRI^b brain images with slice thickness of 2.00 or 3.00 mm and space between slices of 2.20 or 3.20 mm were used. Image slices for each dog were interpolated such that 2 new slices were added between every 2 original data slices by the use of quantitative image analysis software.^{22,c} This procedure increased the number of slices and decreased the space between slices for each dog and resulted in updated image dimensions of 512 X 512 X 58 voxels, 512 X 512 X 25 voxels, 512 X 512 X 67 voxels, 512 X 512 X 67 voxels, and 512 X 512 X 52 voxels for dogs 1 to 5, respectively.

Image preprocessing segmentation and meshing

Brain parenchyma and CSF geometry were extracted from the MRI data with a volumetric image segmentation and visualization package.^d Manual segmentation was assisted by repetitive applications of intensity-based thresholding, Otsu threshold, Boolean operators, and arithmetic filters and resulted in separation of types of material (**Figure 3**). Identified types of material were brain tissue (including gray matter and white matter), CSF, and the boundary between the cranium and contents of the cranial cavity (CCBD region); cystic tissue (dog 3); cystic fluid (dog 3); and tumor tissue (dogs 4 and 5).

The stack of image slices containing the segmented 3-D brain geometry for each dog was then exported and converted into a tetrahedral volume mesh with the aid of software (**Figure 4**).^{23,e,f} During this process, the brain geometry was segregated into triangles and grouped on the basis of type of material. Nodes (points that connected the vertices of the triangles created during the meshing process) were used in FEA simulations.

FEA

Analysis of models was conducted by use of FEA software^g with implicit and explicit solver capabilities. The output file provided by the meshing software was used in the generation of an input-control file whereby the analysis type, loading and boundary conditions, and material property definitions were manually assigned to the automatically generated geometry to complete the information needed by the FEA software.

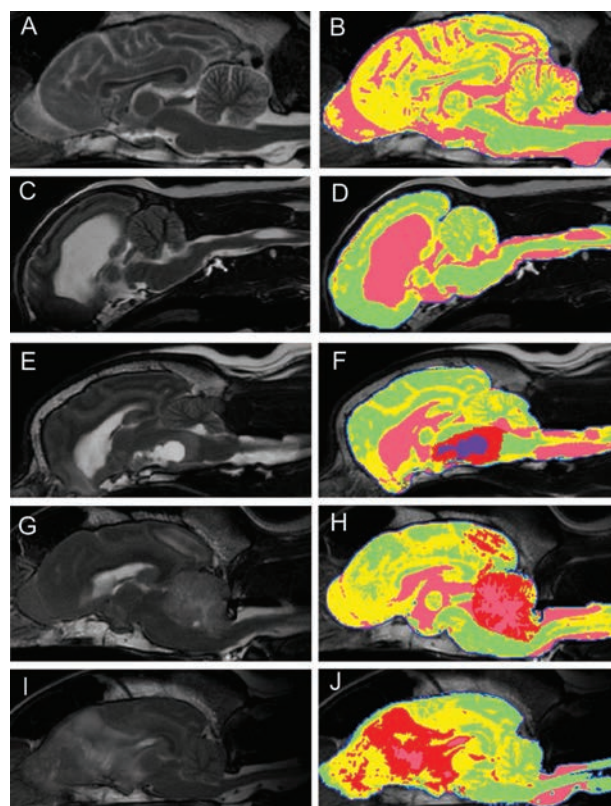


Figure 3—Midsagittal MRI slices for a geometrically normal dog (dog 1 [A and B]) and 4 dogs with brain abnormalities (dog 2, congenital occipital malformation with hydrocephalus and syringohydromyelia [C and D]; dog 3, cystic meningioma in the ventral aspect of the cranial cavity [E and F]; dog 4, cerebellar mass with cerebellar herniation [G and H]; and dog 5, meningioma in the rostral aspect of the cranial cavity [I and J]). Slices were obtained at image acquisition (A, C, E, G, and I), and segmentation masks (B, D, F, H, and J) were created to distinguish material types for all dogs. Cranial cavity contents included brain tissue (yellow and green) and CSF (pink) as well as the boundary between the cranium and contents of the cranial cavity (CCBD [blue]). Additionally, abnormal brain tissue or a tissue mass (red) is visible in dogs 3, 4, and 5 (F, H, and J, respectively), and abnormal cystic fluid (purple) is visible in dog 3 (F).

Simulation of brain parenchyma and CSF

Each brain was modeled as a nonlinear, isotropic, elastic, deformable, and porous material or as a biphasic material composed of a mixture of incompressible permeable parenchyma and nonviscous CSF as the interstitial fluid. The amount of CSF present differed between image slices, dogs, and brain conditions (geo-

metrically normal vs abnormal). In the FEA software, the strain energy (total potential energy) method for material deformation containing both a distortional (deviatoric) and volumetric component of the deformation gradient was defined by the following nonlinear strain energy equation:

$$\rho v_i = (\partial \sigma_{ij} / \partial x_{ij}) + ([1 - \beta T] \rho g_i) - (d[\partial v_i / \partial x_i]) + f_i$$

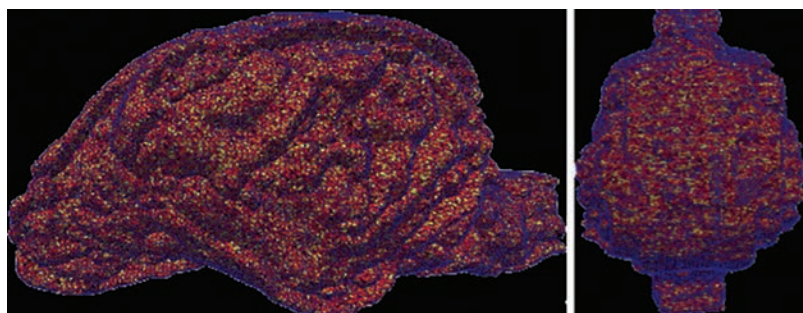


Figure 4—Lateral (left) and caudal (right) views of the model mesh for a geometrically normal canine brain. Nodes are the points that connect vertices of the triangles.

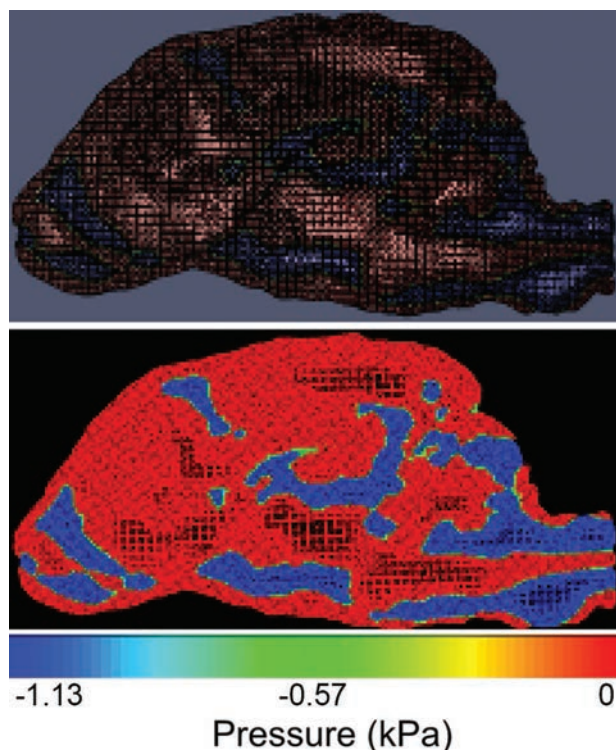


Figure 5—Views of the model mesh for a geometrically normal canine brain superimposed onto the pressure visualization to assist in identifying locations at which pressure (application of 1.13 kPa) is being exerted onto brain tissue by the CSF (top) and by pressure visualization alone (bottom). Locations of pressure origin (blue) correspond to the CSF where the pressure of 1.13 kPa is assigned via the loading conditions in the finite element software. Negative values indicate that the pressure is directed outward from the CSF and onto surrounding brain tissue. Intermediate areas (green) represent boundaries where brain tissue and CSF are in direct contact. The remaining brain tissue and subarachnoid space (red) are regions that are not subjected to pressure because there is no direct contact with CSF.

where ρ is density of the material, v_i is material velocity in the i direction, ∂ is the partial derivative of the function with respect to the space coordinate (x), σ_{ij} is the material stress matrix comprising 9 components representing the state of stress in different directions in 3-D, β is the material expansion volume or measurement of the volume change of a fluid or solid in response to a change in pressure or stress, T is temperature of the material (which was assumed to be constant), g_i is the standard acceleration attributable to gravity, d is the damping coefficient of material (which was negligible because CSF is nonviscous), and f_i is the load tensor source (which was a pressure applied at all nodes within the CSF).

The study was based on the biomechanical response behavior obtained for solving the nonlinear strain energy equation. Mechanical stress (σ), an intensity-level measurement of internal forces acting on the brain parenchyma and CCBD region, is mathematically defined as the force per unit volume. The gradient pressure (CPP) or the pressure associated with CSF (ICP) is responsible for such forces. Strain, or the amount of deformation or volume change the brain undergoes in response to stress, is defined as $\epsilon = \Delta V/V$, where ϵ is strain and V is volume. In this analysis, strain is related to the stress by use of the following equation:

$$\bar{\sigma}_{ij} = \sigma_{ij} - p\epsilon$$

where p is the applied hydrostatic pressure (ICP). The bulk modulus is an expression of material elasticity, which measures the cranial cavity's resistance to changes in volume for an applied pressure by use of the following equation:

$$K = \Delta p / (\Delta V/V)$$

where K is the bulk modulus and Δp is the change in pressure.

Boundary and loading conditions

The geometric approximation provided by the mesh was then supplemented with additional information. This included specifying whether the model was static or moving, whether to account for fluid

flow or temperature factors, or whether forces were acting on or against the model. The following conditions were implemented: each node of the CCBD region was fixed in the x, y, and z directions to mimic its connectivity to the skull; each node of the CSF was fixed in the x, y, and z directions because we were not interested in the flow or movement of CSF but were interested in the location of CSF in each model at the time of image acquisition; and a constant pressure was applied to all nodes within the CSF because the pressure in CSF is the ICP. This pressure was assigned a negative value to simulate a radial force directed outward from the CSF and onto surrounding brain tissue (**Figure 5**). The reference range for ICP in clinically normal dogs ranges from 0.67 to 1.60 kPa (5 to 12 mm Hg)³; therefore, each brain model was subjected to pressures of 0.67, 0.95, 1.13, 1.41, and 1.60 kPa to account for variations within this range. It has been reported^{24,25} that mortality rate increases approximately 20% for each 10 mm Hg decrease in CPP below 70 mm Hg. Low CPP can result in depletion of brain oxygen concentrations, and this lack of perfusion in conjunction with increased ICP is anticipated to affect the biomechanical behavior of both the brain parenchyma and CSF. On the basis of this information, each brain model was additionally analyzed at 2.67, 4.00, 5.33, and 6.67 kPa to mimic 4 incremental 10 mm Hg decreases in CPP (equivalent to 1.33-kPa increases in ICP).

Material properties

Material property values were then assigned to the model to numerically distinguish each material on the basis of strength, elasticity, and durability (from an engineering aspect) as bone, soft tissue, fluid, or a combination of materials^{26–31} (**Appendix 2**). Material composition of the model was important because behavior is dependent on the type of material being examined. Because they were abnormal growths, tumors or abnormal tissue masses were assumed to be slightly more compressible or susceptible to volume changes than was clinically normal brain parenchyma; thus, they were assigned a bulk modulus value of 1.095×10^{-6} kPa and a compressibility value of 9.13×10^{-4} kPa⁻¹. Additionally, the Poisson ratio of 0.35 differed from that of geometrically normal brain tissue. For dog 3, cystic fluid was assumed to be more compressible than CSF and was assigned a Poisson ratio of 0.47 and a compressibility value of 1.90×10^{-3} kPa⁻¹, which corresponded to half the value for the CSF. Although more compressible than CSF, cystic fluid was still considered relatively poorly compressible (compressibility value, approx 0). All material properties for the CCBD region, tumor, abnormal masses, and fluids were estimated for simulation purposes.

Output

The output or visualization step provided solutions and behavioral effects at all points on the model resulting from the simulation conditions im-

posed in conjunction with each brain abnormality present. Behavioral effects included factors such as areas of high stress, high strain, high pressure, or shape distortion. Shape distortion can occur as a result of bending and twisting of the brainstem; swelling of brain tissue; hemorrhaging into brain tissue; blood clotting; obstruction, constriction, dilation, or compression of vessels and ventricles within the brain; or skull fractures resulting from traumatic injury. These results were displayed in the original geometry with 1 specific biomechanical property (ie, stress or strain magnitude) superimposed in a false-color scheme based on a ranking scale of minimum to maximum numeric values as well as tabular charts or line plots of quantitative data. Viewing software^h allowed visualization of the data output by the FEA software.^g The viewing software accepted many input formats, and we used the visualization toolkit format to exchange data between the FEA software and viewing software. Geometry of the midline sagittal slice was used to display visualization results.

Biomechanical behavior attributable to changes in CPP and ICP

An initial experiment was conducted to analyze changes in the biomechanical behavior of a geometrically normal brain. Finite element analysis was performed to simulate changes in stress and strain for ICPs within the reference range for dogs (0.67 to 1.60 kPa) and decreases in CPP in increments of 10 mm Hg (approx 1.33 kPa). Because this decrease in CPP was commensurate with an increase in ICP, the ICP was increased from 1.60 kPa in 4 increments (approx 1.33 kPa/increment) in each simulation to determine the manner in which this increase affected stress and strain distribution behaviors in the model. This incremental pressure increase was based on 2 assumptions: that there is a constant MAP of 90 mm Hg (approx 12 kPa) and that ICP increases the more CPP deviates from MAP because of the mathematical relationship $CPP = MAP - ICP$. Data were recorded for pressures of 0.67, 0.95, 1.13, 1.41, 1.60, 2.67, 4.00, 5.33, and 6.67 kPa.

Biomechanical behavior of geometrically normal versus abnormal brains

An FEA was performed to determine the manner in which brain abnormalities and disorders of various severities affected biomechanical behavior within the cranial cavity. Thus, the preceding experiment conducted on the geometrically normal brain was repeated for each of the abnormal brains. Results for the abnormal brains were compared with those obtained for the simulation with the geometrically normal brain.

Identification of critical values

In an attempt to identify critical values of ICP, stress, or strain that indicated onset of nonlinearity or decompensation, the maximum stress and strain at each pressure were plotted for each abnormal con-

dition. Relationships between these variables were graphed for each condition such that biomechanical response and changes in deformation patterns leading up to this point could be evaluated. On the basis of this information, critical values for each condition at which herniation would possibly occur were identified. Each condition was then assigned a severity ranking on the basis of the rate at which critical pressure, stress, and strain were reached.

Cranial cavity boundary condition comparison

Each abnormal condition was additionally subjected to FEA simulation at an ICP of 1.13 kPa in which only the outermost boundary nodes of the CCBD region were fixed in the x, y, and z directions to mimic connectivity to the skull. Internal nodes of this region were granted free movement in all directions. Data were compared with values reported for simulations at the same pressure under the original boundary conditions to determine the manner in which this affected the biomechanical response behavior.

Statistical analysis

The percentage difference between the maximum stress and strain of dog 1 versus dogs 2 to 5 was calculated at each pressure. Means of the percentage differences were tabulated to evaluate patterns of stress and strain behavior in each abnormal dog in comparison with the geometrically normal dog. No further statistical analysis was performed because only 1 geo-

metrically normal brain and 1 of each brain geometric abnormality were examined.

Results

Relationships between CPP, ICP, and biomechanical response behavior

As CPP decreased from 11.33 to 9.33 kPa and ICP increased from 0.67 to 2.67 kPa, the corresponding maximum stress and strain increases were proportionally linear (**Table 1**; **Figure 6**). The increasing ICP exerted by the CSF caused increased stress on the brain parenchyma, which ultimately increased the amount of strain or deformation. However, nonlinearity was evident immediately at $CPP < 9.33$ kPa (70 mm Hg) and $ICP > 2.67$ kPa (20 mm Hg). Analysis of the intersections of CPP and ICP indicated that CPP had no MAP component (ie, $MAP = 0$ mm Hg because $CPP = ICP$). Under such conditions, it can be assumed that

Table 1—Changes in stress and strain in the brain of a geometrically normal dog as a result of a decrease in CPP or increase in ICP.

CPP (kPa)	ICP (kPa)	Maximum stress (kPa)	Maximum strain
11.33	0.67	1.74	3.01×10^{-6}
11.05	0.95	2.46	4.28×10^{-6}
10.87	1.13	2.93	5.12×10^{-6}
10.59	1.41	3.66	6.38×10^{-6}
10.40	1.60	4.15	7.23×10^{-6}
9.33	2.67	6.92	1.17×10^{-5}
8.00	4.00	10.4	1.64×10^{-5}
6.67	5.33	13.8	2.09×10^{-5}
5.33	6.67	17.3	2.59×10^{-5}

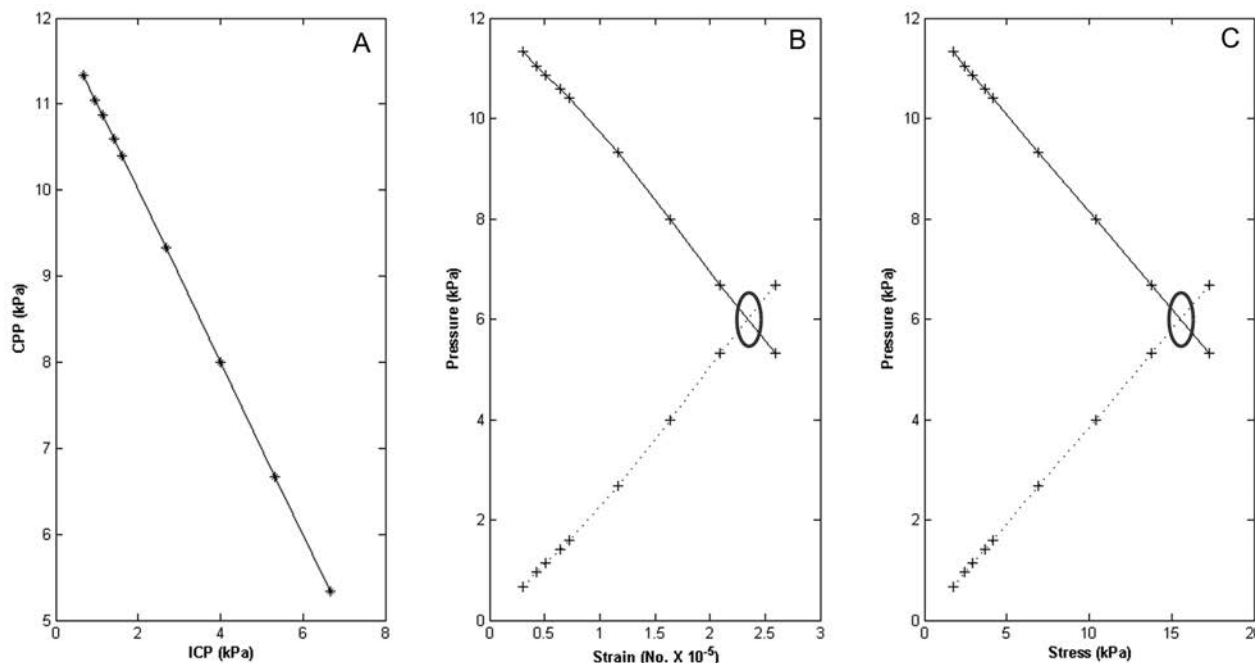


Figure 6—Graphs depicting relationships between ICP and CPP (A), pressure and strain (B), and pressure and stress (C) in the model for a geometrically normal canine brain. In panel A, CPP is described by the mathematical relationship $CPP = MAP - ICP$; thus, as the CPP decreases, the ICP increases. In panels B and C, changes in stress and strain as a result of decreases in CPP (solid line) or increases in ICP (dashed line) are linear. Intersection of the CPP and ICP (circle) represents the pressure at which $CPP = ICP$ and is indicative of an MAP of 0 mm Hg. At an MAP of 0 mm Hg, there is minimal or no blood flow to the brain.

there would be no blood flow and that serious or fatal effects have occurred or are imminent.

Comparison of biomechanical response behavior in geometrically normal and abnormal brain models

Overall, the maximum strain or amount of deformation reported was extremely small (10^{-7} to 10^{-5}) in comparison with the magnitude of the maximum stress (10^3). Variations of differences between maximum stress and strain for each abnormal brain in comparison with results for the geometrically normal brain emphasized that the presence of injury or a medical condition contributed to deformation of the brain tissue at all pressures. The maximum stress for dog 2 differed from that for dog 1 by a mean of 33.61%, with a maximum strain difference of 22.00%. The maximum stress for dog 3 differed from that for dog 1 by a mean of 16.90%, but maximum strain for dog 3 had the largest difference (67.16%) from that of dog 1. Dog 4 had the smallest mean difference in maximum stress (16.76%), compared with that for dog 1, but the maximum strain for dog 4 differed by 27.92%

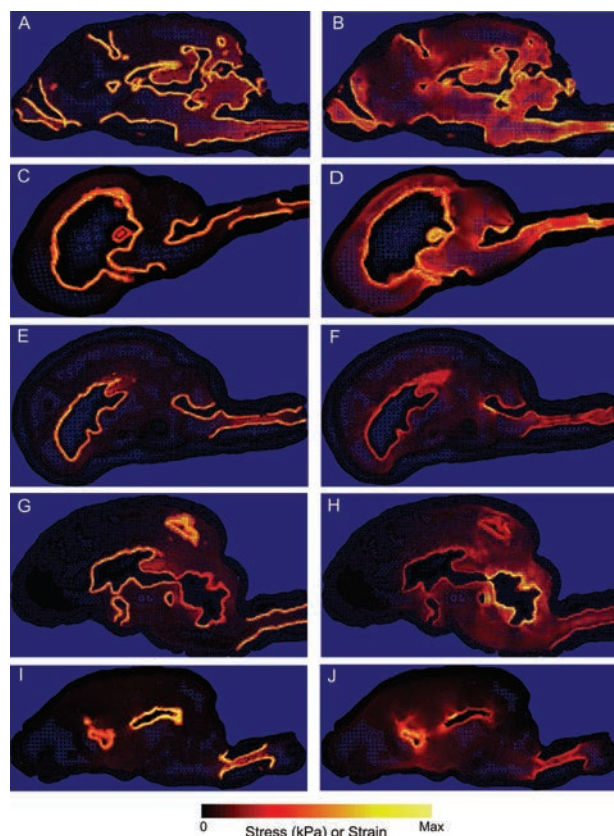


Figure 7—Images for finite element simulation at a pressure of 1.13 kPa of the brains of a geometrically normal dog (dog 1 [A and B]) and 4 dogs with brain abnormalities (dog 2 [C and D], dog 3 [E and F], dog 4 [G and H], and dog 5 [I and J]) that depict the distribution of the response behavior for biomechanical stress (A, C, E, G, and I) and strain (B, D, F, H, and J). The locations of maximum stress and strain (yellow) correspond to boundaries between tissue and fluid. Max = Maximum.

from that for dog 1. The maximum stress and strain for dog 5 differed from those of dog 1 by a mean of 28.16% and 47.97%, respectively. Additionally, assessment of the FEA visualizations of biomechanical response behaviors revealed noticeable differences in distribution patterns of stress and strain (**Figure 7**). However, these response behaviors corresponded to the contact locations of CSF and tissue as well as the abnormalities for each dog (Figure 3); stress and strain were concentrated in the areas where CSF was in contact with tissue and abnormalities were present.

Assessment of critical values and severity of condition

Assorted graphical visualizations of the biomechanical response behavior data obtained from FEA simulations, in conjunction with numeric data, were used to approximate the critical pressure and maximum stress and strain for each abnormal condition (**Figure 8**). Dogs 2 to 5 each had observable nonlinearities detected around critical ICP at approximately 0.95 kPa. Dog 3 had the largest critical value for stress at approximately 2.16 kPa, followed by dog 4 (approx 2.09 kPa) and then dogs 2 (approx 1.86 kPa) and 5 (approx 1.76 kPa). However, dog 2 had the largest critical value for strain at approximately 3.38×10^{-6} , which was followed by dog 4 (approx 3.08×10^{-6}), dog 5 (approx 2.51×10^{-6}), and dog 3 (approx 2.14×10^{-6}). On the basis of the observed relationships between pressure and strain, dog 3 was classified as the most severely affected, followed by dogs 4, 5, 2, and 1. Given the restricted space of the brain cavity in conjunction with results for the critical strain evaluation, deformation limits for each model or the instant at which deformation began in response to increasing stress (ie, elasticity) also confirmed the severity rankings.

Boundary condition effects on biomechanical response behavior

Both maximum stress and strain for each abnormal condition whereby the internal nodes of the CCBD were granted free movement were mostly smaller than those for fully fixed CCBD conditions. Free movement stress and strain values for the geometrically normal dog were 2.01 kPa and 3.21×10^{-6} , respectively, compared with the fixed condition stress and strain values reported at the corresponding pressure (1.13 kPa; Table 1). Dog 2 was the only animal in which the free movement stress value of 2.15 kPa was larger than the fixed condition value of 2.11 kPa; the strain values for free movement and the fixed condition were 1.64×10^{-6} and 3.96×10^{-6} , respectively. For free movement, dogs 3 and 4 had identical stress values of 1.86 kPa (strain values, 1.46×10^{-6} and 1.66×10^{-6} , respectively), compared with values of 2.56 kPa (strain value, 2.57×10^{-6}) and 2.48 kPa (strain value, 3.67×10^{-6}) when internal nodes of the CCBD were fixed. Dog 5 had stress and strain values of 1.89 kPa and 1.70×10^{-6} , respectively, for free movement and 2.21 kPa and 3.10×10^{-6} , respectively, for the fixed

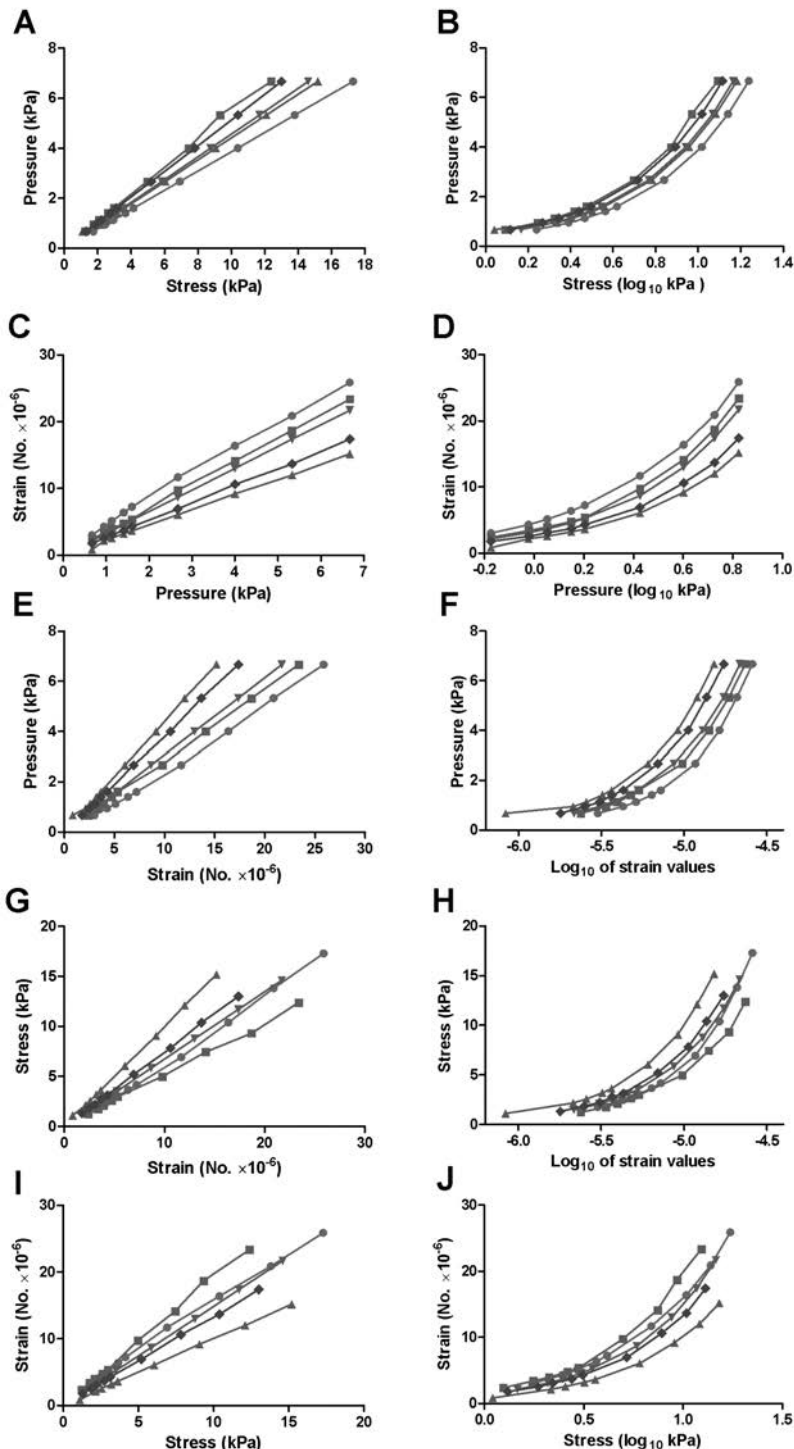


Figure 8—Linear and logarithmic-linear graphs of intracranial stress, strain, and pressure curves used to estimate the critical pressure, stress, and strain for the 5 dogs of Figure 3 (dog 1 [circles], dog 2 [squares], dog 3 [triangles], dog 4 [inverted triangles], and dog 5 [diamonds]). In all dogs, stress increases linearly as the pressure increases (A and B). The relationship between pressure and strain can be used to assist in the classification of injuries or conditions on the basis of an increase (C and D) or decrease (E and F) in severity of injury. Stress and strain curves provide information about patterns or type of nonlinearity (G and I) and are a measurement of elasticity (H and J). Notice that the pattern for the logarithmic scale of the x-axis for the pressure-strain curve (D and F) or stress-strain curve (H and J) resembles the pressure-volume graph.

condition. Additionally, corresponding FEA visualizations of biomechanical response behavior distribution patterns were similar (data not shown). The only noticeable difference was that the stress color map was slightly more visible in the brain parenchyma and more detectable along the CCBD.

Discussion

Intracranial finite element models have been implemented to analyze the deformation and constitutive behavior of brain tissue. These models have been used to provide results for conditions of increased ICP attributable to traumatic brain injury and intracranial conditions such as hydrocephalus^{18,20,21,28,29,32-37} and for prediction of tissue motion during surgical intervention.^{19,30,31,38-41}

To our knowledge, the study reported here was the first in which diagnostic imaging-based FEA was performed on the basis of canine brain anatomy. Additionally, we used 3-D models of the geometry of the complete brain for analysis, rather than using symmetric inferences based on fractions or sections of brain or creating models from single slices of diagnostic imaging data. It seemed logical that analysis of a single MRI slice or isolated section of the brain would be insufficient for simulation, evaluation, and detection of changes in global biomechanical response behavior associated with brain injury attributable to trauma, seizures, hematoma, stroke, tumors, thrombosis, or congenital or acquired ventriculomegaly or hydrocephalus. Our data were provided as midline sagittal cross sections by use of viewing software^h to provide views of biomechanical responses in the subarachnoid space, cerebellum, and brainstem, which are critical for assessment of ICP because herniation, shifts, and compression in these areas can be fatal. Flexibility of the visualization software allowed data to be provided in all sagittal, coronal, and transverse planes.

The initial proportionally linear increases in stress and strain relative to increases in ICP and decreases in CPP (Figure 6; Table 1), compared with the established relationships between pressure and volume, verified that the autoregulatory mechanisms attempted to maintain equilibrium during episodes of increased ICP or a decreasing pressure gradient CPP. The data also pro-

vided a biomechanical validation of the effects of decreases in CPP and increases in ICP within the brain cavity. Both the ICP and differences in CPP indicated the usefulness of the FEA method for noninvasive assessment of ICP and CPP.

Observable changes in biomechanical response behavior based on an abnormality or deformity in instances of increased ICP confirmed that the response behavior (ie, increases in both maximum stress and strain) was dependent on the material types examined. In addition, increases of the mean difference of maximum stress relative to increases in the mean difference of maximum strain for each abnormality, compared with values for the geometrically normal brain, indicated the nonlinear deformation behavior of biomechanical tissues. Stress for each abnormality represented an effect of the amount of CSF present as well as its distribution pattern, given that the pressure acting on the brain parenchyma was exerted by the fluid. In contrast to our initial assumption that the cranial cavity and CCBd region would be the only sites at which the largest amounts of stress and strain would be evident, the biomechanical behavior of any given area within the cranial cavity was affected by the pressure exerted on it (Figure 7).

Assessment of stress-strain relationships in the present study also provided insights into the determination of critical values in which nonlinearity, triggered by cessation of autoregulation mechanisms, began and therefore allowed estimation of the cranial stress, strain, and ICP at which herniation would occur. Anatomic geometry ascertained from diagnostic images permitted this evaluation to be condition-specific and afforded the opportunity to assess whether stress and strain distribution values and behavior characteristics could be classified on the basis of origin or cause of increased ICP or brain volume. This is advantageous over other studies^{18,20,21,27-42} in which investigators implemented FEA with diagnostic imaging to solely focus on specific types of traumatic impact injuries or a specific medical condition (ie, hydrocephalus, tumor, stroke, or aneurysm).

The conclusion that dog 3 reached the critical strain first at low critical stress and pressure was justified by the fact that the combination of the less elastic abnormal tissue and more compressible fluid disrupted the brain volume and resulted in higher stress and earlier onset of deformation, compared with results for the other abnormal conditions (Figure 8). The severity ranking of dogs 4 and 5 obtained from the graphical data could be debated on the basis of the diagnosis reported and visual output provided. For dog 4, the presence of less elastic abnormal tissue in the cerebellum placed the brain on the verge of herniation. This was evident by the ventral and caudal orientation of the cerebellum, compared with the orientation of a geometrically normal brain. A visible impending herniation (dog 4) was expected to be much more severe; however, it is likely that the larger size and distribution of the less elastic tumor tissue distributed throughout

the brain tissue of dog 5 resulted in deformation at lower stresses for increasing ICP. This difference in geographic locations of abnormalities was reflected in the graphical results, even though the critical pressure for each condition was approximately equal.

Dog 2, which had congenital hydrocephalus, had less brain mass because of the large accumulation of CSF in the lateral ventricles. This was a result of the autoregulation mechanisms in the brain compensating for the increased volume of CSF. Additionally, the graphical behavior observed at the higher pressures was likely also the result of CSF contributions. The brain cavity was subjected to large deformations at smaller stresses because of the pressure exerted by the CSF, which was confirmed through assessment of critical stress and strain. On the basis of the results for each abnormality, the pressure, stress, and strain at which a brain model reaches nonlinearity could be used as a critical value or as a potential method to predict the onset of herniation or severity of injury.

The relationship between pressure and strain assisted in the classification of injuries or conditions in accordance with increasing or decreasing severity. Stress and strain curves provide information about the patterns or type of nonlinearity and are a measurement of elasticity. Additionally, application of a logarithmic scale on 1 axis of a pressure-strain or stress-strain curve bears resemblance to the pressure-volume graph (Figure 1). Furthermore, the slope of the strain-stress curve is the compressibility, which measures the relative change in volume of a fluid or solid as a response to a change in mean stress and corresponds to the definition of compliance obtained by the inverse slope of the pressure-volume curve. These relationships represent examples of the reason that the total potential energy finite element concept is ideal for analysis of the cranial cavity.

Although maximum stress and strain were lower when nodes of the CCBd region were free to move, all of the biomechanical response behaviors were still evident, except that the actual magnitude of critical stress and strain would change (brain tissue was subjected to lower amounts of stress, and the strain was lower). The magnitude of strain (10^{-6}) was the same for both node conditions; therefore, dramatic differences in shapes or patterns for graphs were not anticipated.

Deviation of ICP has been used to classify stages of brain injury.⁴² When the ICP deviation is 2.5 kPa, the brain is assumed to be in a state of mild injury. At deviations of approximately 3.5 kPa, the brain reaches a moderate injury threshold, and deviations ≥ 5 kPa are indicative of severe injury. Coincidentally, for all conditions, analysis was performed at ICPs approximately equal to these predetermined injury threshold values. Distinguishable changes in biomechanical property behavior in the form of numeric values may be associated with individual classification for a variety of brain abnormalities or deformities. This further highlighted the potential for FEA, diagnostic imaging, and biome-

chanical distribution response to be used as diagnostic, treatment, and prevention guidelines in clinical settings. From this information, a diagnostic standard can be implemented to estimate ICP and define the state of brain injury on the basis of the response behavior. The ability to noninvasively measure ICP and associate it with a state of brain injury could be a valuable assessment tool for diagnosis, prevention, or treatment in clinical veterinary settings where invasive methods of ICP measurement are rarely used. Because the response behavior mimics that of pressure and volume, the stress-strain conceptual relationships can be easily understood by clinical personnel.

The proposed method for ICP evaluation reported here does have limitations. Manual segmentation of the brain geometry for MRI images is a tedious task that requires an excessive commitment of time, which would ostensibly hinder its integration into clinical practice. Different levels of pixel intensity based on the patient, slice artifacts (eg, noise), or imaging modality used may result in minor misclassification of materials. In addition, the computational time and computer memory required for analysis (use of a 3-D model) may also be a factor; however, the FEA software used in the present study can be linked with libraries that have multithread capabilities, with a corresponding reduction in execution time. For the present study, each model had to be scaled to 45% of its original size to reduce the number of nodes and elements so that the FEA software could operate within memory constraints of our computers. Resizing did not compromise integrity of the data for several reasons. Experiments were conducted to establish a proof of principle; therefore, data obtained at full model size would be proportional to that in the present study. This can be attributed to the fact that stress and strain are substantially more dependent on the materials than on the size of the model.

Additionally, the pressures reported represented instantaneous mean ICP and not the triphasic sinusoidal waveform measurements commonly obtained for ICP measurements, given that mean ICP was used in the calculation of CPP. During the present study, the simulation of CSF flow was not considered; results were based on a static location and the amount of CSF in each slice of data at the time of image acquisition. The cranial portion of the cervical vertebrae was also not considered. In most clinical patients with increased ICP where structural change is evident on MRI or CT images, brain herniation through the foramen magnum or supratentorial herniation is the common manifestation of fatal ICP increases. Relief from increased ICP via the cervical vertebrae or through the central canal was negligible, and imaging data of each dog's brain did not include a consistent portion of the cranial portion of the cervical vertebrae.

Finally, no mechanical testing was performed to verify or validate the numeric model because the assumed nonlinear elastic behavior of brain tissue has long been widely accepted and the medical condition

or diagnosis for each dog was known prior to analysis. The observed pressure gradient and distribution behavior between the brain parenchyma, ventricles, and CCBD region corresponded to results previously reported in other studies.^{36,43,44} However, no published numeric models related to secondary brain injuries (such as those for the dogs of the present study) were available to assist in the validation process.²¹

The objective of the study reported here was to determine whether there was a relationship between the FEA, biomechanical response, and ICP that could be applied to any patient with a brain disease or injury regardless of the cause. This study represented the first step in development of an accurate, reliable, and clinically applicable method for detecting increases in ICP that will enable clinicians to diagnose, treat, and prevent secondary brain injury before irreversible structural changes occur. In patients with a history of trauma, clinicians are more alert to signs of increased ICP and secondary brain injury. In this study, our focus was the development of a noninvasive method for detecting increased ICP regardless of the inciting cause. We have provided a framework for noninvasive estimation of ICP and CPP on the basis of diagnostic imaging data and 3-D consolidation of fluid-solid interaction analysis via the FEA method. Our initial goal was to specifically focus on the brain-skull interface, considering that volume expansion leads to compression of brain parenchyma against the skull. For this method, we relied on biomechanical properties of the brain (ie, stress and strain) to enable us to identify and, in some cases, verify areas of the brain most rapidly and most severely affected by the onset and progression of an increase in ICP and decrease in CPP. Patient scenarios differed. However, these data supported the ability of the method to accommodate various shapes and volumes of cranial cavities associated with medical conditions, age, and breed differences through the use of canine brain models. Future research will revolve around objectives that assist or allow for rapid, automated evaluation of patients in clinical settings; these objectives include identification of more rapid, automated methods of segmentation and adjustment of mesh size; exploration of registration techniques to create atlas databases containing anatomic brain models of assorted species and breeds for segmentation of brain geometry for diagnostic imaging data and anatomic brain models of various injuries and medical conditions (eg, tumors and hydrocephalus) for segmentation of brain geometry from diagnostic imaging data⁴⁵; investigation of techniques, if available (ie, algorithms), that are capable of predicting, obtaining, and assigning mechanical properties on the basis of the geometry and intensity in a diagnostic image to improve patient-specificity in analysis; and implementation of mechanical testing procedures for the purposes of obtaining updated material property values for assorted brain tissue abnormalities and developing numeric models for the validation and veri-

fication of secondary brain injuries that will lead to more realistic and accurate nonlinear modeling and simulation parameters.

Acknowledgments

This manuscript represents a portion of a dissertation submitted by Dr. Madison to the University of Georgia College of Engineering as partial fulfillment of the requirements for a Doctor of Philosophy degree.

Footnotes

- a. Marmarou A. *A theoretical model and experimental evaluation of the cerebrospinal fluid system*. PhD thesis. College of Engineering, Drexel University, Philadelphia, Pa, 1973.
- b. 3-T, 16-channel fixed-site Signa HDx magnet, General Electric, Fairfield, Conn.
- c. Crystal Image, Mark A. Haidekker, Athens, Ga. Available at: www.haidekker.org/cimage/. Accessed Feb 28, 2014.
- d. Seg3D, Scientific Computing and Imaging Institute, University of Utah, Salt Lake City, Utah. Available at: www.seg3d.org. Accessed Feb 28, 2014.
- e. BioMesh3D, Scientific Computing and Imaging Institute, University of Utah, Salt Lake City, Utah. Available at: www.biomesh3d.org. Accessed Feb 28, 2014.
- f. Cleaver, Scientific Computing and Imaging Institute, University of Utah, Salt Lake City, Utah. Available at: www.sci.utah.edu/cibc-software/cleaver.html. Accessed Feb 28, 2014.
- g. Tochnog, Finite Element Application Technology VOF, Heerlen, The Netherlands. Available at: tochnog.sourceforge.net. Accessed Feb 28, 2014.
- h. Paraview, Kitware Inc, Clifton Park, NY.

References

1. Bratton S, Chestnut R, Ghajar J, et al. Guidelines for the management of severe traumatic brain injury. VIII. Intracranial pressure thresholds. *J Neurotrauma* 2006;24:S55-S58.
2. Rangel-Castillo L, Gopinath S, Robertson CS. Management of intracranial hypertension. *Neurol Clin* 2008;26:521-541.
3. Dewey CW. Head trauma management (chapter 6). In: *A practical guide to canine and feline neurology*. 2nd ed. Ames, Iowa: Wiley-Blackwell. 2008;223.
4. Piper I. Intracranial pressure and elastance. In: Reilly PL, Bullock R, eds. *Head injury: pathophysiology and management*. 2nd ed. Boca Raton, Fla: CRC Press, 2005;93-112.
5. Ryder HW, Espey FF, Kristoff FV, et al. Observations on the interrelationships of intracranial pressure and cerebral blood flow. *J Neurosurg* 1951;8:46-58.
6. Popovic D, Khoo M, Lee S. Noninvasive monitoring of intracranial pressure. *Recent Patents Biomed Eng* 2009;2:165-179.
7. Zhong J, Dujovny M, Park HK, et al. Advances in intracranial pressure monitoring techniques. *Neurol Res* 2003;25:339-350.
8. Pattinson K, Wynne-Jones G, Imray CHE. Monitoring intracranial pressure, perfusion and metabolism. *Contin Educ Anaesth Crit Care Pain* 2005;5:130-133.
9. Smith M. Monitoring intracranial pressure in traumatic brain injury. *Anesth Analg* 2008;106:240-248.
10. Raboel P, Bartek J, Andresen M, et al. Intracranial pressure monitoring: invasive versus non-invasive methods—a review. *Crit Care Res Pract* [serial online]. 2012;2012:950393. Available at: www.hindawi.com/journals/ccrp/2012/950393/. Accessed Feb 28, 2014.
11. Marmarou A, Shulman K, LaMorgese J. Compartmental analysis of compliance and outflow resistance of the cerebrospinal fluid system. *J Neurosurg* 1975;43:523-534.
12. Marmarou A, Shulman K, Rosende RM. A nonlinear analysis of the cerebrospinal fluid system and intracranial pressure dynamics. *J Neurosurg* 1978;48:332-344.
13. Sivaloganathan S, Tenti G, Drake J. Mathematical pressure volume models of the cerebrospinal fluid. *Appl Math Comput* 1998;94:243-266.
14. Miller J, Garibi J. Intracranial volume/pressure relationships during continuous monitoring of ventricular fluid pressure. In:

- Brock M, Dietz H, eds. *Intracranial pressure*. Berlin: Springer-Verlag, 1972;270-274.
15. Miller JD, Garibi J, Pickard JD. Induced changes of cerebrospinal fluid volume: effects during continuous monitoring of ventricular fluid pressure. *Arch Neurol* 1973;28:265-269.
16. Kurtcuoglu V, Poulidakos D, Ventikos Y. Computational modeling of the mechanical behavior of the cerebrospinal fluid system. *J Biomech Eng* 2005;127:264-269.
17. Wittek A, Miller K, Kikinis R, et al. Patient-specific model of brain deformation: application to medical image registration. *J Biomech* 2007;40:919-929.
18. Dutta-Roy T, Wittek A, Miller K. Biomechanical modelling of normal pressure hydrocephalus. *J Biomech* 2008;41:2263-2271.
19. Miller K, Wittek A, Joldes G, et al. Modelling brain deformations for computer-integrated neurosurgery. *Int J Numer Method Biomed Eng* 2010;26:117-138.
20. Yang KH, King AI. Modeling of the brain for injury simulation and prevention. In: Miller K, ed. *Biomechanics of the brain*. New York: Springer, 2011;91-110.
21. Yang KH, Mao H, Wagner C, et al. Modeling of the brain for injury prevention. In: Bilston LE, ed. *Neural tissue biomechanics*. Berlin: Springer-Verlag, 2011;69-120.
22. Haidekker M. Image analysis and visualization software (chapter 14). In: *Advanced biomedical image analysis*. Hoboken, NJ: John Wiley & Sons, 2011;456-461.
23. Bronson JR, Levine JA, Whitaker RT. Lattice cleaving: conforming tetrahedral meshes of multimaterial domains with bounded quality, in *Proceedings*. 21st Int Meshing Roundtable 2013;191-209.
24. Changaris DG, McGraw CP, Richardson JD, et al. Correlation of cerebral perfusion pressure and Glasgow Coma Scale to outcome. *J Trauma* 1987;27:1007-1013.
25. McGraw C. A cerebral perfusion pressure greater than 80 mm Hg is more beneficial. In: Hoff JT, Betz AL, eds. *Intracranial pressure VII*. Berlin: Springer-Verlag, 1989;839-841.
26. Lin S, Shieh S, Grimm M. Ultrasonic measurements of brain tissue properties, in *Proceedings*. Symp Centers Dis Control Prevent 1997;27-31.
27. Yang J. Investigation of brain trauma biomechanics in vehicle traffic accidents using human body computational models. In: Wittek A, Nielsen PMF, Miller K, eds. *Computational biomechanics for medicine*. New York: Springer, 2011;5-14.
28. Omori K, Zhang L, Yang KH, et al. Effect of cerebral vasculature on the mechanical response of brain tissue: a preliminary study, in *Proceedings*. ASME Int Mech Eng Cong Exposition 2000;246:167-174.
29. Kaczmarek M, Subramaniam RP, Neff SR. The hydromechanics of hydrocephalus: steady-state solutions for cylindrical geometry. *Bull Math Biol* 1997;59:295-323.
30. Miller K. Constitutive model of brain tissue suitable for finite element analysis of surgical procedures. *J Biomech* 1999;32:531-537.
31. Dassios G, Kiriakopoulos M, Kostopoulos V. On the sensitivity of the vibrational response of the human head. *Comput Mech* 1998;21:382-388.
32. Nagashima T, Tamaki N, Matsumoto S, et al. Biomechanics of hydrocephalus: a new theoretical model. *Neurosurgery* 1987;21:898-904.
33. Tada Y, Matsumoto R, Nishimura Y. Mechanical modelings of the brain and simulation of the biomechanism of hydrocephalus. *Trans Jpn Soc Mech Eng* 1990;33:269-275.
34. Jacobson EE, Fletcher DF, Morgan MK, et al. Fluid dynamics of the cerebral aqueduct. *Pediatr Neurosurg* 1996;24:229-236.
35. Peña A, Bolton MD, Whitehouse H, et al. Effects of brain ventricular shape on periventricular biomechanics: a finite-element analysis. *Neurosurgery* 1999;45:107-116.
36. Taylor Z, Miller K. Reassessment of brain elasticity for analysis of biomechanisms of hydrocephalus. *J Biomech* 2004;37:1263-1269.
37. Linninger AA, Xenos M, Zhu DC, et al. Cerebrospinal fluid flow in the normal and hydrocephalic human brain. *IEEE Trans Biomed Eng* 2007;54:291-302.

38. Gilchrist M, O'Donoghue D. Simulation of the development of frontal head impact injury. *Comput Mech* 2000;26:229-235.
39. Gong S, Lee H, Lu C. Computational simulation of the human head response to non-contact impact. *Comput Struc* 2008;86:758-770.
40. Li Z, Luo Y. Finite element study of correlation between intracranial pressure and external vibration responses of human head. *Adv Theor Appl Mech* 2010;3:139-149.
41. Valencia A, Blas B, Ortega JH. Modeling of brain shift phenomenon for different craniotomies and solid models. *J Appl Math* [serial online]. 2012;2012:409127. Available at: www.hindawi.com/journals/jam/2012/409127/. Accessed Feb 28, 2014.
42. Yue X, Wang L, Wang R. Tissue modeling and analyzing with finite element method: a review for cranium brain imaging. *Int J Biomed Imaging* [serial online]. 2013;2013:781603. Available at: www.hindawi.com/journals/ijbi/2013/781603/. Accessed Feb 28, 2014.
43. Levine DN. Intracranial pressure and ventricular expansion in hydrocephalus: have we been asking the wrong question? *J Neurol Sci* 2008;269:1-11.
44. Levine DN. The pathogenesis of normal pressure hydrocephalus: a theoretical analysis. *Bull Math Biol* 1999;61:875-916.
45. Kyriacou SK, Davatzikos C, Zinreich SJ, et al. Nonlinear elastic registration of brain images with tumor pathology using a biomechanical model. *IEEE Trans Med Imaging* 1999;18:580-592.

Appendix I

Characterization of brain response for various increases in the ICP.

ICP	Response
Compensation	
Level I	Reduction in amount of CSF by increase in reabsorption rate; vasoconstriction
Level II	Increase in blood pressure through systemic constriction of arteries in an effort to overcome the high ICP and ultimately increase the CPP
Decompensation	
Level III	Severe depletion of oxygen in brain; increase in blood flow to brain
Level IV	Herniation or displacement of brain tissue, blood vessels, and CSF through the foramen magnum

Appendix 2

Material property values used in finite element simulation.

Property	Brain	Cerebrospinal fluid	CCBD*	Reference
Density (kg/m ³)	1.04 × 10 ³	1.00 × 10 ³	1.04 × 10 ³	26
Bulk modulus (kPa)	2.19 × 10 ⁶	1.05 × 10 ⁶	2.10 × 10 ⁶	27
Poisson ratio	4.85 × 10 ⁻¹	4.99 × 10 ⁻¹	4.50 × 10 ⁻¹	28-31
Compressibility (kPa ⁻¹)†	4.57 × 10 ⁻⁷	9.52 × 10 ⁻⁷	4.76 × 10 ⁻⁷	NA

*Boundary between the cranium and contents of the cranial cavity. †Calculated as 1/K, where K is the bulk modulus. NA = Not applicable.